Author version

Published as:

Ha, T. H., Lee, K., & Hwang, J. T. (2020). Large-scale multidisciplinary optimization under uncertainty for electric vertical takeoff and landing aircraft. In AIAA Scitech 2020 Forum (Paper No. AIAA 2020-0904). https://doi.org/10.2514/6.2020-0904

BibTeX for this reference:

https://lsdolab.github.io/lsdo-publications/publication/ha2020large/


```
@inproceedings{ha2020large,
  author = {Tae H. Ha and Keunseok Lee and John T. Hwang},
  title = {Large-scale multidisciplinary optimization under uncertainty for electric
    vertical takeoff and landing aircraft},
  booktitle = {AIAA Scitech 2020 Forum},
  year = {2020},
  doi = {10.2514/6.2020-0904},
  url = {https://doi.org/10.2514/6.2020-0904}
}
```

Large-scale multidisciplinary optimization under uncertainty for electric vertical takeoff and landing aircraft

Tae H. Ha*
University of California, San Diego, La Jolla, CA, 92093

Keunseok Lee†
Hyundai Motor Company, Seoul, Korea

John T. Hwang‡
University of California, San Diego, La Jolla, CA, 92093

Urban air mobility is a growing field of research that holds potential to transform commuting options in congested cities. Electric vertical takeoff and landing (eVTOL) concepts are well-suited as design choices for this field considering noise, space, and environmental benefits. In this paper, we demonstrate large-scale multidisciplinary design optimization (MDO) of eVTOL aircraft at a system level, minimizing power required during hover. By including operational variables, we determine the feasibility of an eVTOL concept's design parameters in varying cruise and hover mission specifications. Using Uber's common reference model (eCRM) 001, we observe a 9.66% decrease in peak power usage when optimizing design parameters in addition to operational variables. By incorporating thrust power margin as model uncertainty, we determine an eVTOL design that significantly increases robustness with a relatively minor penalty to efficiency.

I. Introduction

Electric aircraft and the corresponding literature have been on the rise for the past few years. From 2006 to around 2009, roughly one paper per year was being published concerning electric and hybrid electric aircraft design and analysis, while from 2015 to 2018, this number rose to nearly 20 per year [1]. The advantages of electric aviation are largely environmental benefits, as emissions are lower, overall efficiency of the propulsion system is multiple times higher, and noise is lower with electric motors.

The energy densities of today's batteries present a bottleneck for electric aircraft in terms of range. With current-generation batteries, pure electric propulsion is not feasible for regional airliners and larger commercial aircraft due to range limitations. Hybrid-electric propulsion has the potential to increase the range to an acceptable level, but it introduces complexity and loses some of the benefits of electric propulsion, e.g., simplicity, reliability, and lower maintenance costs. As a result, much of the initial research in electric aviation focuses on urban air mobility (UAM), which is the transportation of people, goods, and services within a city using 1-4 passenger aircraft. Vertical takeoff and landing (VTOL) capability is critical for UAM, giving rise to the term, eVTOL.

There is a wide range of eVTOL concepts being considered for UAM. Given that concepts, technologies, and operational models are evolving simultaneously for UAM, a rapid computational design capability is especially beneficial. One approach is multidisciplinary design optimization (MDO), which has been an active field of research for over two decades [2]. MDO refers to the use of numerical optimization, which is the minimization of an output with respect to design variables subject to constraints.

In the past couple of years, there have been several studies that apply design optimization approaches to electric aircraft design. Borer and Moore [3] perform design exploration of the integrated propeller-wing system for high-lift performance for NASA's X-57 demonstrator aircraft for distributed electric propulsion (DEP). Moore and Ning [4] perform MDO of an electric aircraft using blade element momentum theory (BEMT) and a vortex lattice method (VLM). Hwang and Ning [5] perform MDO of the X-57 using BEMT, VLM, and 1-D structural finite element analysis (FEA).

*Master's Student, Department of Mechanical and Aerospace Engineering, AIAA Student Member.
†Research Engineer.
‡Assistant Professor, Department of Mechanical and Aerospace Engineering, AIAA Member.

These previous computational design and MDO studies use multidisciplinary, physics-based models that capture many of the key design tradeoffs, enabling an optimization algorithm to automate the process of finding the best design for a given objective. However, a common limitation is that previous applications of MDO to electric aircraft do not have the capability to consider the effect of uncertainties in the model. These uncertainties can be categorized as two types: as aleatory uncertainty (also called irreducible uncertainty or stochastic uncertainty) which is uncertainty due to inherent variation or randomness, or epistemic uncertainty which is uncertainty due to a lack of current state of knowledge.

Uncertainty is not a new concept and has been discussed in nearly all fields, but uncertainty quantification for large-scale multidisciplinary optimization has been relatively new. Researchers such as Liang and Mahadevan [6] have looked into this in response to a challenge sent out by NASA [7] regarding the issue of several correlated topics in uncertainty quantification and propogation for multidisciplinary models. For this paper, we plan to incorportate some uncertainty analysis with large-scale models and apply them for electric vertical takeoff and landing (eVTOL) vehicles.

II. Background

In this section, we cover the background information necessary regarding electric aircraft classification and hazard identification in Sec. II.A. In Sec. II.B, we go over the OpenMDAO framework, which we will use to construct our electric aircraft model. We review related previous work done in Sec. II.C regarding uncertainty quantification pertaining to multidisciplinary systems.

A. Electric Aircraft Architecture

While multiple variations of what is classified as 'electric aircraft' exist, these differences can be classified by the degree of hybridization with respect to power and energy through

$$H_P = \frac{P_m}{P_{tot}} \tag{1}$$

$$H_E = \frac{E_b}{E_{tot}}, \tag{2}$$

where P_m is the motor power while E_b is the battery energy. [8] All-electric aircraft depend solely on electrical energy for their propulsion, where $H_p = 1$, $H_E = 1$. Hybrid electric aircraft depend on a varying ratio of fuel and electrical energy, where $H_p > 0$, $0 < H_E < 1$. Turbo-electric aircraft use electric generators to convert the mechanical energy of their turbines into electric energy, which then is used to power the propulsion system; with no battery component, $H_E = 0$ and $H_p > 0$. Conventional aircraft use no electric power and energy, thus $H_P = H_E = 0$. For this paper we will be working solely with all-electric aircraft models.

When applying optimization for electric aircraft, uncertainty quantification is significant when dealing with the importance of safety and design. Courtin et al. [9] discuss emerging hazards and categorizes different them based on hazard consequence levels ranging from negligible (little to no effect on aircraft, occupants, and flight crew) to catastrophic (normally hull loss and multiple fatalities) while simultaneously identifying probability levels as expected number of failures per flight hour from extremely improbable ($< 10^{-7}$) to probable ($< 10^{-3}$) for multi-engined aircraft with 2-4 passengers. This is illustrated in Fig. 1, showing a risk matrix with hazard consequences levels versus probability levels. These hazards were further analyzed with respect to different electric aircraft architectures based on how the vehicle generates lift and whether or not the vehicle utilizes some form of distributed propulsion. The four main groups used for evaluating the different hazards were multirotor vehicles, distributed electric propulsion (DEP) powered-lift aircraft, fixed-wing vehicles, and rotorcraft (which do not use DEP).

Courtin et al. found that the significant emerging hazards based on risk severity (probability x consequence) were battery thermal runaway, battery energy uncertainty, common mode power failure, fly-by-wire system failure, high-level autonomy failure, and bird strike. The key hazards to note here are battery thermal runaway and high-level autonomy failure which both hold high risk severity for all the architecture groups listed, whereas the other risks hold either lower risk severity overall or varying risk severity based on the aircraft architecture. High-level autonomy failure regards the need for sophisticated systems to account for the current direction of pilotless operations that urban air mobility is heading towards. Proposals to solve this issue involve advanced machine learning algorithms and will not be covered in the scope of this paper. Battery thermal runaway involve internal short circuits lead to rapid, uncontrollable bursts of heat, which can result in fire or a battery explosion. This effect can be caused by a number of factors, but the primary one

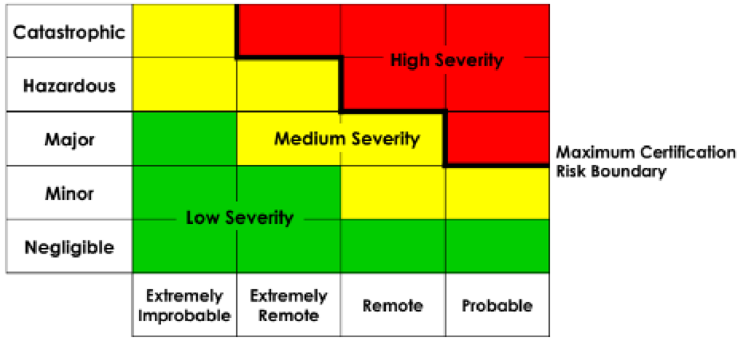

Fig. 1 Risk matrix showing high-(red), medium-(yellow), and low-(green) severity risk areas.[9]

we can work with is over-heating, which we can account for more reliability using risk constraints involving uncertainty. This effect can also be dealt with using physical containment strategies which mitigate the possibility of this hazard at the cost of weight penalties. These weight penalties reduce the effective specific energy of the battery, the uncertainty and effects of which we will be observing in our optimizations.

B. OpenMDAO framework

For large-scale optimization, efficient computation techniques are needed, especially when considering system-level problems. Given the combined requirements of system-level modeling with large-scale optimization, a modular approach is critical where the framework automates part of the effort for computing derivatives.

For these requirements, we use OpenMDAO [10] which simplifies this task. Given a set of model inputs, design variables, constraints, and objective function, OpenMDAO framework solves linear systems using the adjoint method, encapsulated in the equation

$$\frac{\mathrm{d}f}{\mathrm{d}x} = \frac{\partial F}{\partial x} - \frac{\partial F}{\partial y}\left[\frac{\partial R}{\partial y}\right]^{-1}\frac{\partial R}{\partial x}, \tag{3}$$

where f is the output variable, F is the output function (where $f = F(x,y)$), x is the set of input variables, y is the set of state variables, r_y is the set of residual values, and R is the set of residual functions (where $r_y = R(x, y)$). All partial derivatives here are taken as functions with respect to arguments, while total derivatives are taken with variables with respect to other variables. Determining that

$$\frac{\mathrm{d}f}{\mathrm{d}r_y} = -\frac{\partial F}{\partial y}\left[\frac{\partial R}{\partial y}\right]^{-1}, \tag{4}$$

through some algebraic operations,

$$\frac{\partial R}{\partial y}^T \frac{\mathrm{d}f}{\mathrm{d}r_y}^T = -\frac{\partial F}{\partial y}^T \tag{5}$$

can be configured. This can be substituted into Eq. (3), giving us

$$\frac{\mathrm{d}f}{\mathrm{d}x} = \frac{\partial F}{\partial x} + \frac{\mathrm{d}f}{\mathrm{d}r_y}\frac{\partial R}{\partial x}, \tag{6}$$

giving us a linear system to solve for with no dependencies on the number of design variables n_x, and instead proportional to the number of quantities of interest, n_f. [11] This works identically to the vector of constraint values v and vector of constraint functions V, where instead

$$\frac{\mathrm{d}c}{\mathrm{d}x} = \frac{\partial C}{\partial x} + \frac{\mathrm{d}c}{\mathrm{d}r_y}\frac{\partial R}{\partial x}, \tag{7}$$

giving us the length of vector c computations to run. While computing total derivatives may be easier solved with this adjoint method or simply chain rule, other issues from optimization such as coupling occurs, which OpenMDAO handles with its Modular Analysis and Unified Derivatives (MAUD) architecture, based centrally around the Unified Derivatives Equation:

$$\left[\frac{\partial \mathcal{R}}{\partial u}\right]\left[\frac{\mathrm{d}u}{\mathrm{d}r}\right] = \left[I\right] = \left[\frac{\partial \mathcal{R}}{\partial u}\right]^T \left[\frac{\mathrm{d}u}{\mathrm{d}r}\right]^T, \tag{8}$$

where u denotes the vector of all the variables within the model (i.e. every output of every component) and

$$\mathcal{R}(o) = \begin{pmatrix} x - x* \\ -R(x, y) \\ f - F(x, y) \\ c - C(x, y) \end{pmatrix}, \tag{9}$$

where $\mathcal{R}(o) = 0$. With this, all analytic derivative computations from direct to adjoint to chain rule are simplified and allow for simple and efficient processing.

While this MAUD architecture represents the core of OpenMDAO, other modes are available to allow for further robustness. Finite difference methods are available for computing derivatives in case analytic partials cannot be specified prior, and both gradient-based and gradient-free models such as sequential least squares programming (SLSQP) and constrained optimization by linear approximation (COBYLA) are available respectively. The internal solver is by default the NewtonSolver (implements Newton's method), but can also be specified to use other algorithms such as NonlinearBlockGS (applies Block Gauss-Seidel, mainly for cyclic connections), ArmijoGoldsteinLS(checks bounds and backtracks until the Armijo–Goldstein condition is met), and multiple others. The variability of the framework allows for modeling of low-fidelity projects such as been used with OpenAeroStruct, an open-source aerostructural analysis and optimization tool. [12]

C. Uncertainty quantification

Running any uncertainty quantification measures for large-scale multidisciplinary models leads to issues regarding the curse of dimensionality for error propogation, and while uncertainty quantification is by no means a new field, research in applying such analysis to large-scale models or for eVTOL aircraft is fairly minimal. Yao et al. [13] introduce the utilization of uncertainty multidisciplinary design optimization (UMDO) to improve the robustness of the design of a small satellite using a Monte Carlo method. Yao et al. [14] continue to review the UMDO solving process from theory preliminaries to uncertainty modeling and analysis techniques. Jaeger et al. [15] explore aircraft MDO under both model and design variable uncertainty using a low-fidelity analytical model built from Monte Carlo simulations. Vasquez and Rivas [16] covers uncertainty propagation using an initial mass uncertainty for two cruise conditions using a generalized polynomial chaos (GPC) method. Hu et al. [17] review Monte Carlo methods and applications for aerospace vehicles, covering Bayesian inference, importance sampling, Latin hypercube sampling (LHS), and meta-modeling approximation based Monte Carlo simulation. Peherstorfer et al. [18] explore large-scale uncertainty propogation using a multifidelity Monte Carlo approach that leverages low-cost low-fidelity models to reduce computational cost. Uncertainty quantification for an eVTOL aircraft is a relatively unexplored domain that we will couple along with our design optimization.

III. Methodology

A. Discipline models

1. Atmospheric model

The atmospheric model computes temperature, pressure, density, speed of sound, Reynolds number, and dynamic pressure, all as a function of altitude (Fig. 2). UAM aircraft would not fly in the stratosphere; however, for completeness, the model in Fig. 2 incorporates the stratosphere and uses cubic interpolants to create a smooth transition from the troposphere to the stratosphere.

Temperature is assumed to vary linearly with altitude in the troposphere with no consideration of local weather. Given temperature, pressure is computed by integrating the hydrostatic equation, replacing density with an expression involving pressure and temperature using the ideal gas law. Density is then computed using the ideal gas law, and the

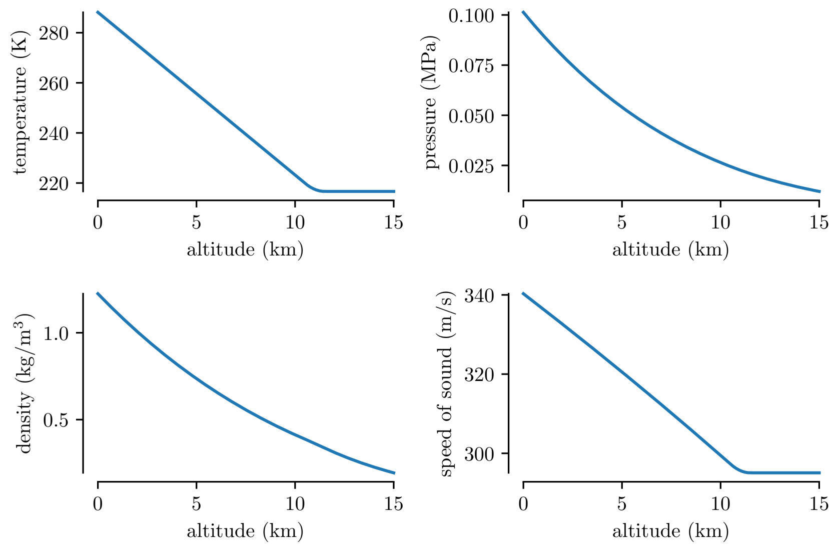

Fig. 2 Temperature, pressure, density, and speed of sound as a function of altitude [19].

speed of sound and viscosity simply from temperature. Reynolds number and dynamic pressure are computed using their well-known definitions.

We show the equations for only the stratosphere here. Temperature as a function of altitude is given by

$$T(h) = T_0 - L \times h \tag{10}$$

where $T_0 = 288.16\,\mathrm{K}$ is the temperature at sea level and $L = 6.5\,\mathrm{K/km}$ is the lapse rate. Pressure as a function of altitude is given by

$$p(h) = p_0 \left(\frac{T(h)}{T_0} \right)^{\frac{g}{LR}} \tag{11}$$

where $p_0 = 101325\,\mathrm{Pa}$ is the pressure at sea level, $g = 9.81\,\mathrm{m/s^2}$ is the acceleration due to gravity, and $R = 287\,\mathrm{m^2/s^2/K}$ is the gas constant. Given the temperature and pressure, we can easily compute density from the ideal gas law using

$$\rho = \frac{p}{RT}, \tag{12}$$

and the speed of sound using

$$a = \sqrt{\gamma R T}, \tag{13}$$

where $\gamma = 1.4$ and again, $R = 287\,\mathrm{m^2/s^2/K}$. Viscosity is given by

$$\mu = \mu_r \left(\frac{T}{T_r} \right)^{1.5} \frac{T_r + T_s}{T + T_s}, \tag{14}$$

where $T_r = 273.15K$ is the reference temperature, $T_s = 110.4K$ is the Sutherland temperature, and $\mu_r = 1.716 \times 10^{-5}$kg/m/s is the viscosity at the reference temperature.

2. *Vortex lattice method*

The vortex lattice method (VLM) is considered a low-fidelity aerodynamic model for predicting the lift, induced drag, and moment of lifting surfaces. VLM models make three key assumptions about the flow—that it is incompressible, inviscid, and irrotational. It represents wings using structured meshes that extend in two dimensions (chord-wise and span-wise).

Assumptions. The inviscid assumption means that the VLM cannot capture viscous drag (skin friction drag). For the resultant aerodynamic forces derived from pressure rather than shear forces on the surface, we are assuming that the viscous effects are pre-dominantly present in the boundary layer, and we are only analyzing the flow outside of the boundary layer. For any resultant aerodynamic forces derived from shear forces on the surface, i.e., skin friction drag, we must combine the VLM with another model that can capture skin friction drag. The incompressible assumption is the prescription of constant density. This is valid when $M < 0.3$, and this is indeed the case for typical UAM missions. The irrotational assumption follows from the inviscid assumption. Vorticity is defined as $\xi = 2\omega = \nabla \times V$. It is a conserved quantity because of the conservation of angular momentum, and in the absence of viscous forces, there is no mechanism to create vorticity.

Potential flow. Applying the incompressible assumption to the continuity equation leads to the deduction that the gradient of velocity is zero, or $\nabla \cdot V = 0$. The irrotational assumption can be mathematically stated as $\nabla \times V = 0$, which means the velocity field can be described using a velocity potential, or $V = \nabla \phi$. Combining these two observations, we obtain Laplace's equation, or $\nabla^2 \phi = 0$. Because of the linearity of Laplace's equation, we can apply the superposition principle, and define flow fields by finding and summing multiple solutions of Laplace's equation. For the VLM, we require only two types of solutions: uniform flow and the flow around vortex filaments.

A vortex filament is a mathematical construction that consists of any number of piecewise line segments. It cannot end in the flow, so it must extend to infinity at both ends. A vortex filament has a constant strength throughout, i.e., the circulation, and it is said to 'induce' a flow field around it. We can use Biot–Savart's law to compute the flow velocity at any point in 3-D due to the given vortex filament. The net flow velocity due to the vortex filament is the sum of the flow velocities due to all the line segments that make up the vortex filament, which can be finite, semi-infinite, or infinite.

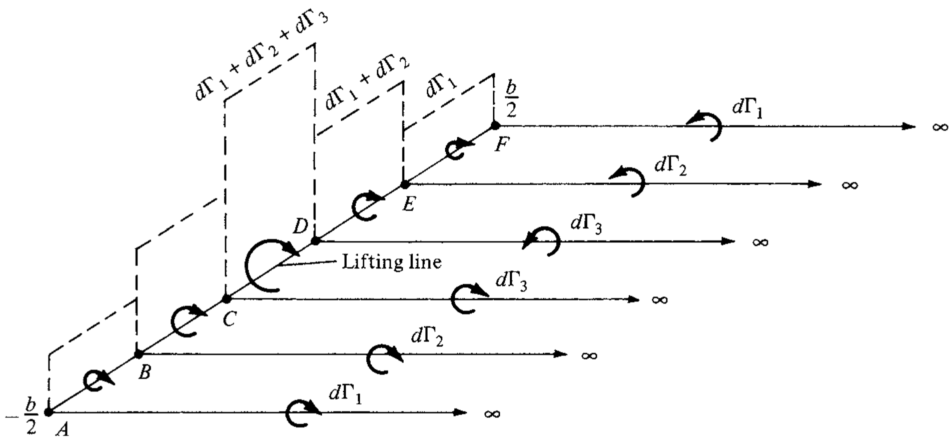

Fig. 3 Representation of a wing using horseshoe vortices [20].

Formulation. In the VLM, lifting surfaces are modeled using a set of horseshoe vortices, as shown in Fig. 3. They are positioned so that there is one row of horseshoe vortices as in Fig. 3 for each set of chord-wise panels in the VLM mesh, and the semi-infinite legs of the horseshoe vortices follow the chord-wise edges of the VLM mesh. For each quadrilateral 'panel' in the VLM mesh, the bound vortex (the finite span-wise segment of each horseshoe vortex) is located at the quarter-chord of the panel.

If there are n panels in a VLM mesh, there are n unknowns—n distinct horseshoe vortices whose strengths must be solved for. These n unknowns are defined by n equations that come from imposing the condition that, in each panel, the flow must be tangent to the panel. This condition is enforced at the three-quarter-chord mark in the middle of the panel in the span-wise direction—the *control point*, as shown in Fig. 4. Mathematically, the condition is a statement that we have a zero dot product of the panel normal vector and then net velocity including the induced velocities due to all the vortex filaments. We have n such equations and n unknowns for the circulations for each horseshoe vortex, and so the

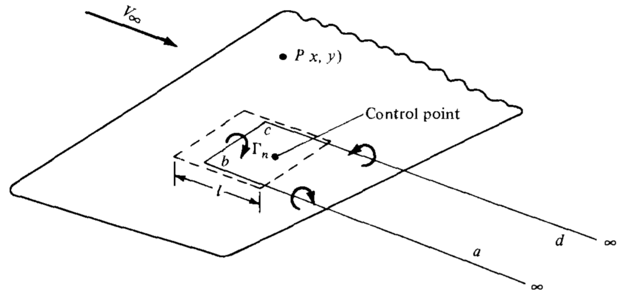

Fig. 4 Representation of a single panel in a VLM mesh [20].

governing equations in the VLM result in a linear system that yields the vector of circulations—the state variables of this model.

3. Blade element momentum theory

Blade element momentum theory (BEMT) is a propulsion model that combines momentum theory, which uses a control-volume analysis and blade element theory, which is based on surrogate models produced off of known airfoil data at discretized sections of local angles of attack. By equating the two theories, the axial and tangential induced velocities can be calculated and thrust, torque, and lift can be predicted. Each propeller is separately modeled and accounted for for both slipstream influence and force and moment equilibrium. The propulsion modeling and airfoil data is implemented and used by Hwang and Ning [5] in the MDO study of NASA's X-57 experimental aircraft demonstrator for distributed electric propulsion (DEP).

4. Dimensionless efficiency metrics

It is useful to consider non-dimensional indicators of rotor efficiency in a way that is independent of scale, rotational speed, and so on. However, there are different metrics that are appropriate for the cruise and hover conditions.

For cruise, we can define *propulsive efficiency*, η, as

$$\eta = \frac{P_{\text{out}}}{P_{\text{req}}}, \tag{15}$$

where P_{out} is the output power and P_{req} is the required power. This expression can be simplified to

$$\eta = \frac{TV}{Q\omega}, \tag{16}$$

where T is thrust, V is forward speed, Q is torque, and ω is angular speed.

For hover, we can define a *figure of merit*, FOM, as

$$FOM = \frac{P_{\text{ideal}}}{P_{\text{req}}}, \tag{17}$$

where P_{ideal} is the ideal power. From momentum theory, we have

$$P_{\text{ideal}} = \frac{C_T^{3/2}}{\sqrt{2}C_P} \tag{18}$$

where, the thrust and power coefficients are respectively defined as

$$C_T = \frac{T}{\rho A V_{\text{tip}}^2} \quad \text{and} \quad C_P = \frac{P_{\text{req}}}{\rho A V_{\text{tip}}^3}, \tag{19}$$

where ρ is the atmospheric density, A is the disk area, and V_{tip} is the blade tip speed.

Validation of the BEMT model was completed by comparing results with CCBlade, a tool for analyzing wind turbine aerodynamic performance that can be reversed for propeller analysis [21]. The propeller design used was a 3-blade rotor with a 1.61 meter radius along with a linear taper chord length from 0.42 to 0.11 meters and linear twist from 34.3 to 14.3 degrees. The propeller was run at two different operating points: during cruise, the nominal RPM and speed were 1800 and 67 m/s respectively, while for hover, the nominal RPM and speed were 794 and 2 m/s respectively. Thrust, torque, power, and efficiency (or figure of merit for the hover point) were the factors of interest, and the trends generally agree for both CCBlade and our current MDO model, as can be seen in Fig. 5.

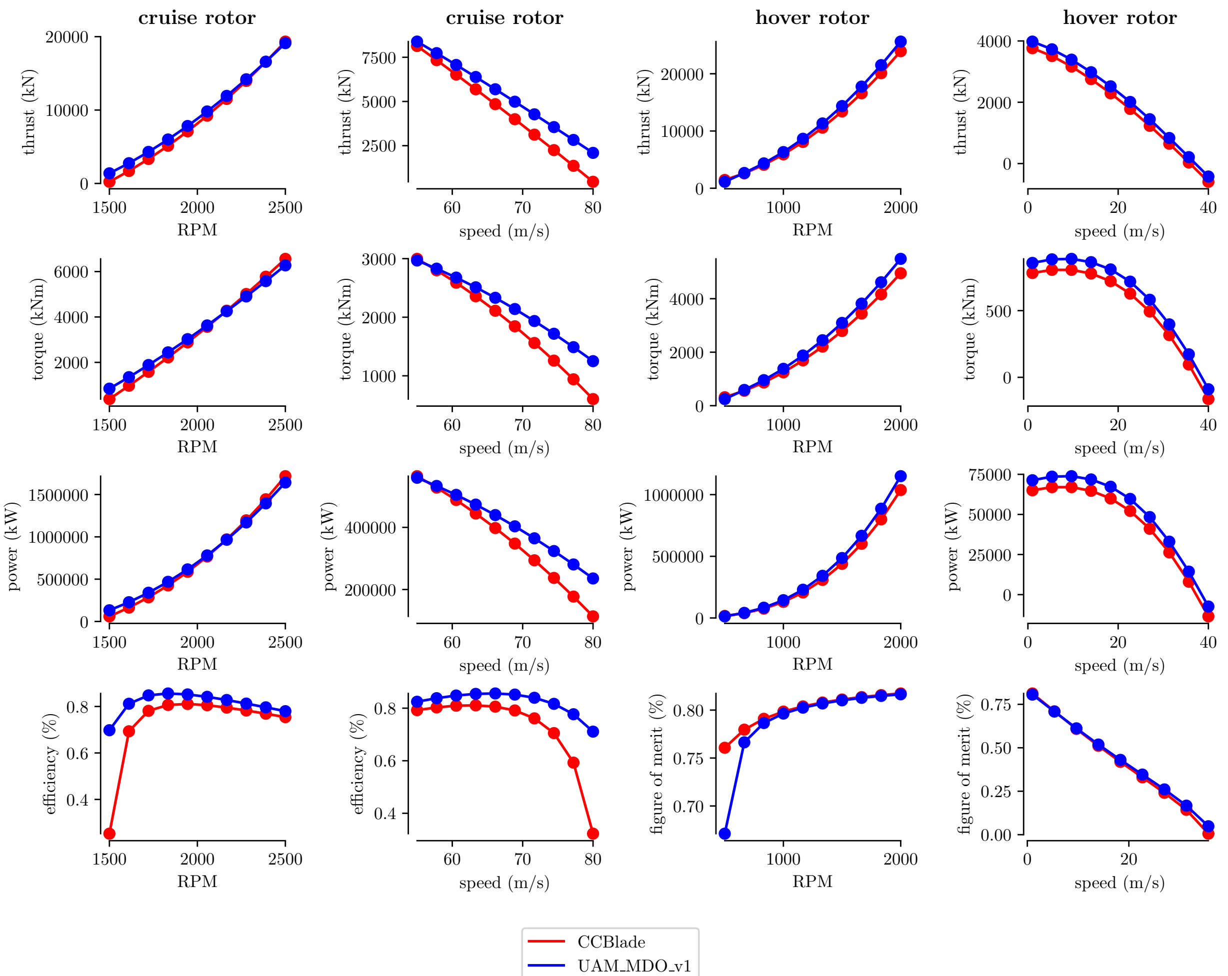

Fig. 5 Thrust, torque, power, and either efficiency (for cruise) or figure of merit (for hover) measured at varying RPMs and speeds.

5. Slipstream model

The induced velocity field in the propellers' slipstream is modeled using analytical approximations. The slipstream contraction is approximated [22] using

$$R(x) = R\sqrt{\frac{1 + a_x}{1 + a_x\left(1 + \frac{x}{\sqrt{R^2+x^2}}\right)}}, \tag{20}$$

which is derived assuming a uniform axial load distribution. As noted by Veldhuis, there are errors in this approximation due to nacelle effects [22], but we use it as a first-order model that is at least better than neglecting slipstream contraction entirely.

For the evolution of the axial and radial components of induced velocity, we use the analytical solution of Conway [23] for elliptically-loaded blades, following Alba [24]. These components are given by

$$V_r(r,x) = V_x(r,0)\left[\frac{|x|R(x)}{2r\sqrt{R(x)^2-r^2}}\left(\frac{1}{a}-a\right) - \frac{r}{2\sqrt{R(x)^2-r^2}}\arcsin\left(\frac{2R(x)}{b}\right)\right], \tag{21}$$

$$V_x(r,x) = V_x(r,0)\left[2 - \frac{aR(x)}{\sqrt{R(x)^2-r^2}} + \frac{x}{\sqrt{R(x)^2-r^2}}\arcsin\left(\frac{2R(x)}{b}\right)\right], \tag{22}$$

where

$$a = \sqrt{\frac{\sqrt{(R(x)^2-x^2-r^2)^2+4R(x)^2x^2}+(R(x)^2-x^2-r^2)}{2R(x)^2}}, \tag{23}$$

$$b = \sqrt{x^2+(R(x)+r)^2}+\sqrt{x^2+(R(x)-r)^2}. \tag{24}$$

The value of $V_x(r,0)$ is computed from $V_x(r,0) = V_{x_0}\sqrt{R(x)^2-r^2}/R(x)$, where V_{x_0} is the axial induced velocity at the disk, averaged radially. The axial velocity component is considered zero for $r > R(x)$. Likewise, the tangential velocity is also considered zero for $r > R(x)$, and since modeling its evolution in x is more complicated, we use a swirl recovery factor (SRF) of 0.5, following Veldhuis [22]. Since we use a constant value of SRF, this model is not well-suited for use for investigating the stream-wise location of rotors relative to the wings to which they are attached. The SRF is a multiplier on the tangential induced velocity computed at the disk and it captures the influence of the wing on dampening the swirl in the slipstream.

Validation of the aero-propulsive model was completed by comparing RANS CFD predictions that use OVER-FLOW, STAR-CCM+, and FUN3D in Fig. 6. The geometry used is NASA's X-57 Maxwell, and was run at two different operating conditions: a cruise condition (unblown) and a high-lift condition (blown). At cruise, only the unpowered aerodynamics is considered to validate again the VLM model as well as the parasitic drag calculation at different angles of attack given a maximum C_l at a cruise speed of 77.2 m/s. For the high-lift setup, slipstream influence due to the propellers is included as well as a Fowler flap set at 30° deflection and 25% additional area modeled using equations for C_L and C_D from Raymer [25]. The unpowered aerodynamics for our current model match well and lie between the turbulent and transition models. For the high-lift configuration, the MDO model follows a similar trend to the CFD data but underpredicts or overpredicts at certain angles of attack by a small margin. On average, the model shows an overall sufficient agreement. The CFD data was obtained from Borer et al. [26] (for cruise) and Deere et al. [27].

6. Parasitic drag model

The parasitic drag model uses the concept of an "equivalent skin friction coefficient" C_{f_e}, obtained from Raymer [25] to include both estimations of skin-friction drag as well as separation pressure drag. To model the skin-friction drag, the most important factor is the extent at which the aircraft has laminar flow across its surfaces. For portions with turbulent flow, an aircraft part can be modeled as a flat-plate where the skin-friction coefficient can be determined by

$$C_f = \frac{0.455}{(\log_{10} R)^{2.58}(1+0.144M^2)^{0.75}} \tag{25}$$

where R is Reynolds number and M is the Mach number, a correction that becomes more trivial at lower speeds. To account for the pressure drag caused by flow separation, a form factor derived from both theoretical and empirical considerations can be used. For subsonic drag, the form factor can be calculated using

$$FF = \left(1 + \frac{60}{f^3} + \frac{f}{400}\right), \tag{26}$$

with f calculated using the below

$$f = \frac{l}{d} = \frac{l}{\sqrt{(4/\pi)A_{max}}}, \tag{27}$$

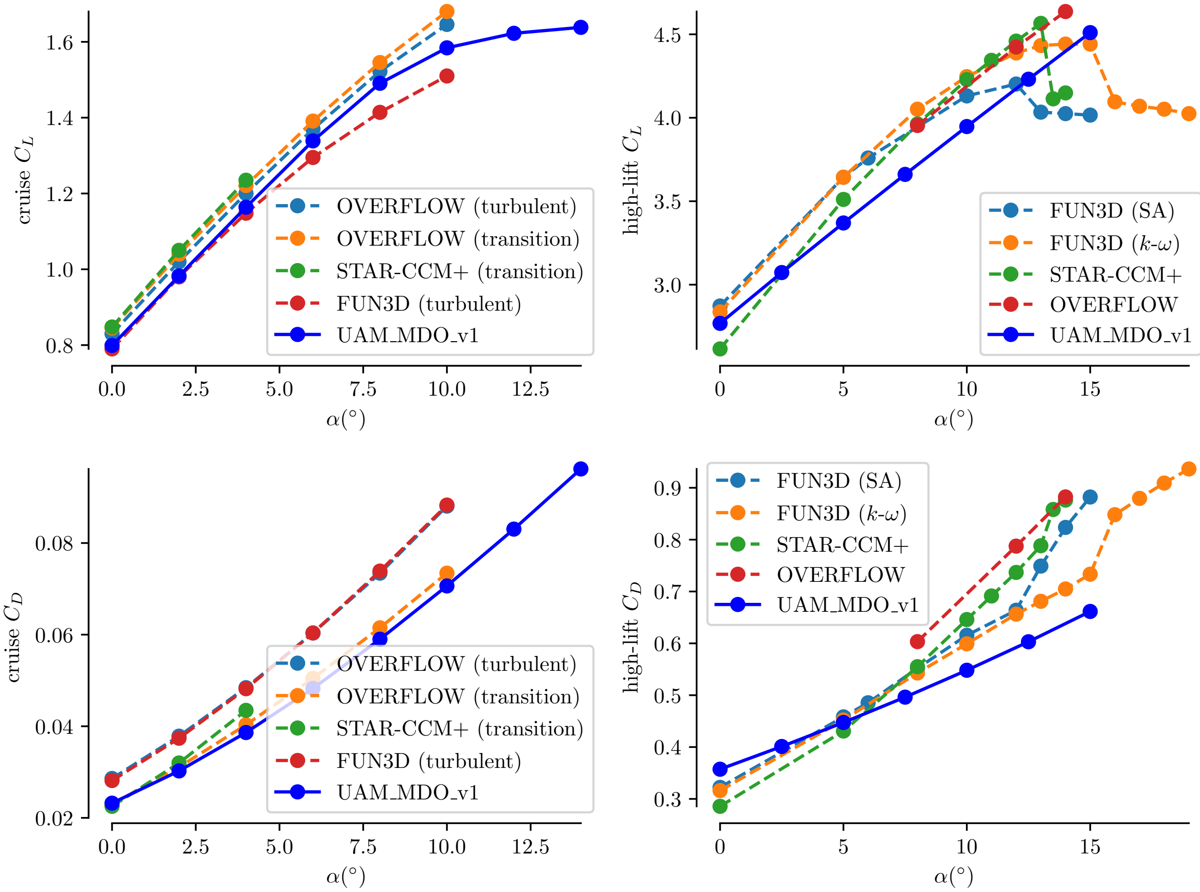

Fig. 6 Unpowered (left) and powered (right) aerodynamics analysis comparing different RANS CFD solvers to our current UAM MDO model at varying angles of attack.

where l and A_{max} represents the length and cross-sectional area of the plate respectively. Parasitic drag also increases due to mutual interference between components. Without the use of more refined aerodynamics tools, preliminary estimations simply involve a percent increase, where for parts mounted directly on the fuselage or wing, the interference factor Q is about 1.5. The fuselage has a negligible intereference factor ($Q = 1.0$) in most cases. The component parasite drag can be now be calculated using the skin-friction coefficient, form factor, and interference factor previously obtained using

$$C_{D_p} = C_{f_e} * Q * FF * \frac{S_{wet}}{S_{ref}}. \tag{28}$$

with S_{wet} and S_{ref} being the component's wetted area and reference area respectively.

7. Weights model

The weights model is based off of several statistical equations obtained through regression analysis used for general aviation from Raymer [25]. A list of the equations used for the weight calculations of the different aircraft components are shown below:

$$W_{fuselage} = 0.052 * S_f^{1.086}(N_z W_{dg})^{0.177} L_t^{-0.051}(L/D)^{-0.072} q^{0.241} \tag{29}$$

$$W_{flightcontrols} = 0.053 * L^{1.536} * B_w^{0.371}(N_z W_{dg} * 10^{-4})^{0.80} \tag{30}$$

$$W_{horizontaltail} = 0.016 * (N_z W_{dg})^{0.414} q^{0.168} S_{ht}^{0.896} \left(\frac{100t/c}{\Lambda}\right)^{-0.12} \left(\frac{A}{\cos^2\Lambda_{ht}}\right) \lambda_h^{-0.02} \tag{31}$$

$$W_{motor} = 9.80665 * \left(-2\text{E}^{-5}P^2 + 0.1595P + 3.3081\right) \tag{32}$$

$$W_{wing} = 0.036 S_w^{0.758} \left(\frac{A}{\cos^2\Lambda}\right)^{0.6} q^{0.006} \lambda^{0.04} \left(\frac{100t/c}{\cos\Lambda}_{-0.3}\right) (N_z W_{dg})^{0.49} \tag{33}$$

All resulting weight calculations here are determined in pounds and are converted to SI units in the running model. Definitions of the terms in the equations can be seen below.

S_f	=	fuselage wetted area (ft^2)
N_z	=	ultimate load factor; = 1.5 X limit load factor
W_{dg}	=	flight design gross weight (lb)
L_t	=	tail length (ft)
L	=	fuselage structural length (ft)
D	=	fuselage structural depth (ft)
q	=	dynamic pressure at cruise (lb / ft^2)
B_w	=	wing span (ft)
S_{ht}	=	horizontal tail area (ft^2)
S_w	=	trapezoidal wing area (ft^2)
t/c	=	thickness-to-chord ratio
Λ	=	wing sweep at 25% of the mean aerodynamic chord (rad)
Λ^{ht}	=	tail sweep at 25% of the mean aerodynamic chord (rad)
A	=	aspect ratio
λ	=	wing taper ratio
λ^h	=	tail taper ratio
P	=	power input (kW)

The motor gear and propeller blade weights are calculated based off a percentage of the motor weight, while the weights of components such as the battery and payload are used as inputs for the model, allowing them to be set as design variables. Due to the coupling involved with some component weights requiring a gross takeoff weight, a nonlinear Gauss-Seidel solver is added (provided by the OpenMDAO framework).

B. Configuration

For the model configuration, we used Uber's electric Common Reference Model (eCRM) model 001. This model is a four passenger + one pilot vehicle that consists of two tilt rotors capable of both forward and vertical flight along with four sets of stacked rotors for solely vertical flight located on the booms and fuselage. Keeping the electric engines near the wings allows for the benefits that DEP provides, and Uber makes use of co-rotating propellers for the stacked rotors that turn in the same direction. This is in contrast with the more commonly seen contra-rotating propellers where each propeller rotates in the opposite direction. Both offer the benefit of added efficiency, however co-rotating propellers decrease noise while contra-rotating increase noise, a feature that is necessary when considering the advantages of using electric aircraft as opposed to conventional.

Uber lists multiple specifications that will be considered its standard for urban air mobility, several of which assisted in formulating the mission parameters for this work. Specifications of the geometry parameters were obtained using a open-source model created in OpenVSP [28], a parametric aircraft geometry tool useable for engineering analysis, and recreated in our CAD-free framework, shown in Fig. 7, to allow for parametrization and exact derivative computation. Current models are insufficient to capture the effects of co-rotating propellers accurately without the use of CFD analysis, and so the stacked rotors are modeled using 4-blade propellers.

Fig. 7 Uber eCRM-001 model (left) and replicated CAD-free model (right).

5 operating conditions are set to formulate the optimization problems:
1) nominal cruise
2) reserve cruise
3) maximum-speed cruise
4) nominal hover
5) hover with one rotor inoperative

The nominal cruise point is set at 150 mph (241 km/h) and is required to fly at least 60 miles (96 km) one-way. The reserve point is set at a lower speed for stall conditions, while the max speed point accounts for airspace sequencing and headwinds. We minimize power input for the nominal hover condition and include an additional emergency condition in hover where a rotor becomes inoperable. For this rotor, the second rotor from the back was chosen (dubbed as rear_rotor_1 in upcoming rotor and performance tables).

C. Optimization setups

1. Large-scale MDO

We consider 5 operating conditions for 3 optimization problems:
1) Mission-only optimization
2) Mission and propeller twist distribution optimization
3) Mission, propeller twist distribution, propeller radius, and wing area optimization

For the mission only optimization, the 5 operating conditions are set with a fixed geometry in terms of wing and rotor sizing as well as propeller shape. The design variables are the operational variables for the aircraft, consisting of the angle of attack, tail trim, propeller blade pitch angle, and rotor rotation speed. Pitch angle is mirrored on pairs of rotors, i.e. the two tilt rotors and hover rotors fixed onto the nacelle, and kept as individual variables for the two rear rotors located on the fuselage. Due to the motor weights sized according to their max power output, the battery weight and position is also included as a design variable to satisfy a center of gravity (CG) constraint. Mission and propeller twist optimization includes the above operational variables as well as several control points defining the propeller twist profile for each set of rotor pairs as well as individual twist profiles for the two rear rotors. The last optimization consists of all of the above design variables set, as well as variable sets of propeller radii and a wing scale factor that stretches the span and chord of the wing while keeping the aspect ratio constant. The formulation of this problem with all design variables included is shown in Tab. 2.

To simplify the problem, constraints for force equilibrium are relaxed between cruise and hover segments; for cruise points, relevant force equilibrium axes are the X (pointing towards the rear of the aircraft) and the Z (pointing above the aircraft) axes, satisfying lift equal to weight and thrust equal to drag. For hover points, only the Z axis is considered to satisfy thrust equal to weight. Similarly, using the same axis orientation, constraints for moment equilibrium are constructed; for cruise points, only the Y axis is considered (along with the CG constraint) to satisfy longitudinal stability. For hover points, moments about both the X axis and Y axis are constrained to account for any roll for the aircraft.

Variable	Lower bound	Upper bound	Count	Notes
minimize				
hover power				
with respect to				
angle of attack	-3°	8°	3	cruise conditions only
tail trim angle	-8°	8°	5	all conditions
blade pitch angle	-10°	55°	20	(2 rotor pairs + 2 separate rotors) × 5 conditions
blade twist offset	-10°	10°	40	(2 rotor pairs + 2 separate rotors) × 10 control points
rotor radius	1.2 m	1.6 m	4	
rotor speed	191 RPM	1910 RPM	30	6 rotors × 5 conditions
battery position	0	5	1	position along x-axis
battery weight	300 kg	800 kg	1	
wing scale factor	-0.02	0.	1	
total design variables			105	
subject to				
range	100 km		1	
CG	3.6896	3.6896	1	
force equilibrium	0	0	8	
moment equilibrium	0	0	7	
tip mach number	0.0	0.6	6	6 rotors
propeller spacing	0	0	2	
total constraints			25	

Table 2 Optimization problem formulation.

Tip mach number is given as an upper bound as a surrogate for noise. A Kreisselmeier-Steinhauser (KS) function is used to evaluate the max tip mach number for each rotor across all missions, decreasing the problem size while still enforcing the constraint at all mission points. To ensure no overlap between propellers occurs, spacing constraints are set in place that take into account both rotor position changing as wing size changes as well as rotor radii sizes.

2. Uncertainty quantification

While finding objective minimal power is important, we consider the possibility of uncertainties within the model. Motor efficiency is always a key factor that is variable to parameters such as temperature that we do not have included in our analysis. We can account model uncertanties by running several similar cases simultaneously while adding some additional model uncertainty distribution. Taking all mission conditions into account, we can set the objective of the optimization to minimize

$$power_{robust} = a * mean(power) + (1 - a) * variance(power), \tag{34}$$

where a is a constant that acts as a weight between desiring an optimal versus robust design. The model parameter we vary is a thrust power margin, using a nominal condition factor of 1, and equally spaced margin factors from 0.7 to 1.3 to optimize 7 different cases in total. By running several different optimizations at various values of a, we can observe the tradeoff that the optimizer must sacrifice in terms of minimizing hover power compared to making the design robust. The formulation of this problem with all design variables included is shown in Tab. 3.

Due to the size of the model already and limited computational resources, these uncertainty-focused optimizations will need to be run separately from the full mission profile optimizations. As such, these results and the accompanying designs should be compared solely with each other and not between the previous optimizations.

D. Optimization algorithm

The optimization problems given in Tab. 2 and 3 are nonlinear programming (NLP) problems. We solve them using SNOPT [29], an active-set sequential quadratic programming (SQP) algorithm, via the aforementioned pyOptSparse package [30]. SNOPT uses a Broyden–Fletcher–Goldfarb–Shanno (BFGS) Hessian approximation, which requires only

Variable	Lower bound	Upper bound	Count	Notes
minimize				
hover_{robust}				
with respect to				
tail trim angle	-8°	8°	7	all conditions
blade pitch angle	-10°	55°	28	(2 rotor pairs + 2 separate rotors) × 7 conditions
blade twist offset	-10°	10°	40	(2 rotor pairs + 2 separate rotors) × 10 control points
rotor speed	191 RPM	1910 RPM	42	6 rotors × 7 conditions
total design variables			117	
subject to				
force equilibrium	0	0	7	
moment equilibrium	0	0	14	
tip mach number	0.0	0.6	6	6 rotors
total constraints			27	

Table 3 Optimization problem formulation.

first derivatives of the model and allows the algorithm to achieve superlinear convergence rates. As shown in Fig. 8, SNOPT solves the optimization problem at the cost on the order of hundreds of model evaluations, and it achieves more than two and six orders of magnitude convergence in optimality and feasibility, respectively.

IV. Results

A. Mission only

The values of the design variables and key quantities of interest are shown in Tab. 4 and 5. For the three cruise missions, the different speeds can be seen, with expected corresponding values for angle of attack and lift to drag ratio. Low speeds require a higher angle of attack to obtain the same lift, leading to a higher lift-to-drag ratio and ultimately lower power required. Likewise, for higher speeds, the opposite is true and is in agreement with the variables and performance shown for the max speed condition. Benefits of a tilt-rotor configuration for the vehicle can already be seen comparing total power between cruise and hover missions; configurations such as helicopters would consume similar amounts of power for both cruise and hover, whereas here the nominal cruise power is less than a third of the nominal hover power required. The power requirements for the five conditions we see here will be the base case to compare alongside the optimizations including design parameters.

Condition	Speed (m/s)	Alpha (deg)	Tail trim (deg)	L/D	C_L	C_D (counts)	Total power (kW)
Cruise	66.67	3.5	-5.88	14.86	0.58	388.34	70.87
Reserve	55.56	6.02	-5.96	16.06	0.83	517.88	56.59
Max. speed	73.76	2.46	-5.86	13.6	0.47	346.74	92.38
Hover	1.0		-7.59				240.65
Hover.OEI	1.0		-7.59				254.48

Table 4 System-level design variables and performance metrics for the optimized design.

Looking at Tab. 5 for the cruise segments, RPM's are kept at nominal values with the other parameters zeroed out for all non-tilt rotors due to being inactive during the cruise missions. For the hover segments, the optimizer places a large portion of the thrust burden onto the fixed rotors, accounting for around 55% of the total thrust. This can be

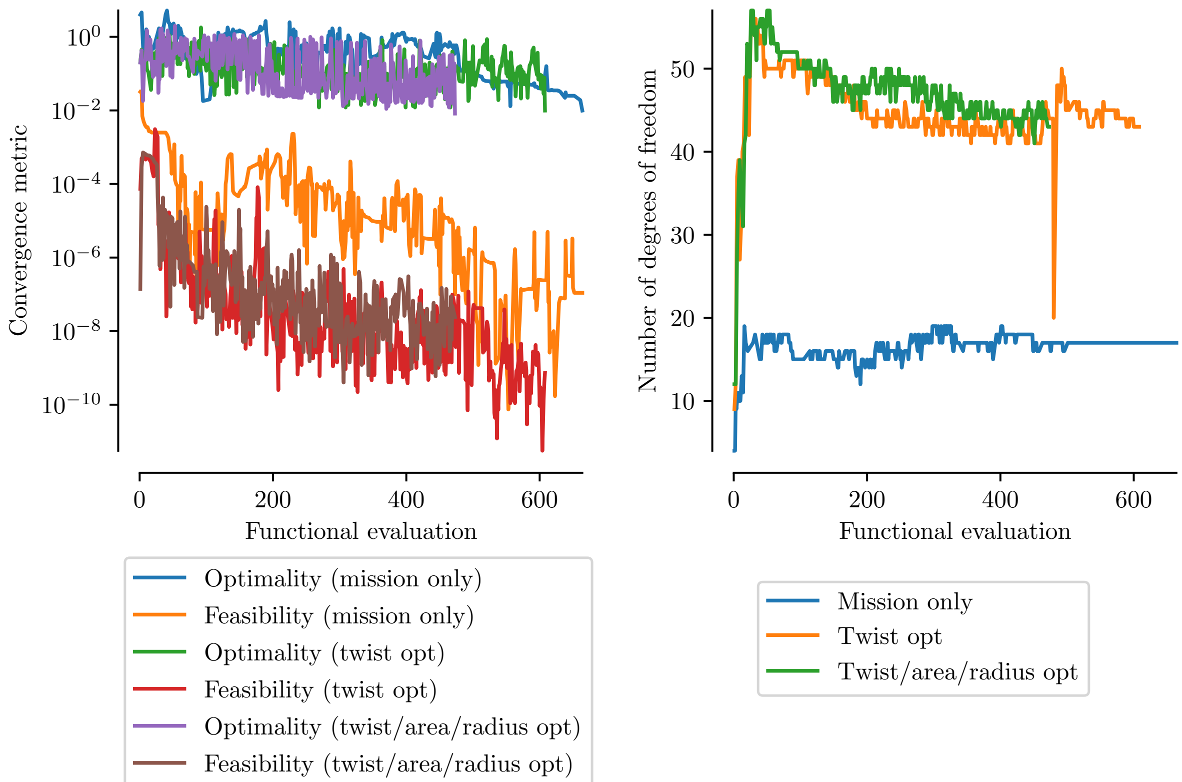

Fig. 8 Optimization convergence history. Optimality is the norm of gradient of the Lagrangian, and feasibility is the norm of the constraint violation. The number of degrees of freedom is the number of design variables that are neither at their bounds nor used to satisfy active constraints—therefore, it is a measure of the dimension of the feasible space.

explained due to the preliminary motor model being used, where increased power usage is not as heavily penalized with additional weight. Because of this, using this model, it is more efficient to place a large emphasis on increasing one set of motor size while keeping other motors low in weight. For the fifth mission condition (one engine inoperable), rear_rotor_1 and its parameters are zeroed out, essentially turning the rotor "off" for the optimizer. The second rear rotor largely accounts for this and more than doubles its thrust to satisfy both force and moment equilibrium. Altogther, rotor variables and parameters are nearly symmetrical and demonstrate reasonable values for a system-level optimization.

B. Mission and propeller twist distribution

The values of the design variables and key quantities of interest are shown in Tab. 6 and 7. The trends for system-level parameters versus cruise speed all show agreement to those seen in the mission only optimization. Compared to optimizing solely with operational variables, we see that optimizing the twist profiles for each set of rotors yields a 7.95% decrease in total power for the nominal hover condition. The optimized blade twist profile shows better efficiency overall towards hover conditions as expected, with the one engine inoperable condition also seeing a decrease in total power of 5.11%. The drawback follows that performance in the cruise missions is worsened, with a 2.23%, 2.56%, and 19.34% increase in total power for the nominal, reserve, and max speed cruise conditions respectively.

Looking at Tab. 6, for the hover conditions, the thrust is now slightly more dispersed across the rotors, with the fixed rotors accounting for 48.92% of the total thrust in the nominal hover case.

Condition	Rotor	RPM	Pitch (°)	Thrust (N)	Torque (Nm)	Power (kW)	Efficiency (%)
Cruise	tilt_rotor_left	402.5	55.0	487.6	840.8	35.4	91.7
Cruise	tilt_rotor_right	402.5	55.0	487.4	840.5	35.4	91.7
Cruise	fixed_rotor_left	983.6	0.0	-0.0	0.0	0.0	
Cruise	fixed_rotor_right	983.6	0.0	-0.0	0.0	0.0	
Cruise	rear_rotor_1	983.6	0.0	-0.0	0.0	0.0	
Cruise	rear_rotor_2	983.6	0.0	-0.0	0.0	0.0	
Reserve	tilt_rotor_left	384.7	52.5	469.4	703.4	28.3	92.0
Reserve	tilt_rotor_right	384.4	52.5	468.0	701.7	28.2	92.0
Reserve	fixed_rotor_left	983.6	0.0	-0.0	0.0	0.0	
Reserve	fixed_rotor_right	983.6	0.0	-0.0	0.0	0.0	
Reserve	rear_rotor_1	983.6	0.0	-0.0	0.0	0.0	
Reserve	rear_rotor_2	983.6	0.0	-0.0	0.0	0.0	
Max. speed	tilt_rotor_left	657.7	41.4	504.0	649.3	44.7	83.1
Max. speed	tilt_rotor_right	662.8	41.4	543.9	686.6	47.7	84.2
Max. speed	fixed_rotor_left	983.6	0.0	-0.0	0.0	0.0	
Max. speed	fixed_rotor_right	983.6	0.0	-0.0	0.0	0.0	
Max. speed	rear_rotor_1	983.6	0.0	-0.0	0.0	0.0	
Max. speed	rear_rotor_2	983.6	0.0	-0.0	0.0	0.0	
Condition	**Rotor**	**RPM**	**Pitch (°)**	**Thrust (N)**	**Torque (Nm)**	**Power (kW)**	**FOM (%)**
Hover	tilt_rotor_left	600.3	4.5	2109.0	681.6	42.8	41.2
Hover	tilt_rotor_right	600.3	4.5	2109.0	681.6	42.8	41.2
Hover	fixed_rotor_left	1608.0	-3.3	3995.7	396.3	66.7	99.7
Hover	fixed_rotor_right	1608.0	-3.3	3995.7	396.3	66.7	99.7
Hover	rear_rotor_1	1065.1	-4.3	1545.4	145.9	16.3	98.3
Hover	rear_rotor_2	726.8	-4.2	715.6	68.9	5.2	96.1
Hover.OEI	tilt_rotor_left	621.9	4.5	2265.8	731.8	47.7	41.2
Hover.OEI	tilt_rotor_right	621.9	4.5	2265.8	731.8	47.7	41.2
Hover.OEI	fixed_rotor_left	1607.3	-3.0	4140.0	419.1	70.5	99.5
Hover.OEI	fixed_rotor_right	1607.3	-3.0	4140.0	419.1	70.5	99.5
Hover.OEI	rear_rotor_1	983.6	15.0	0.0	0.0	0.0	
Hover.OEI	rear_rotor_2	1103.4	-4.3	1658.8	156.3	18.1	98.5

Table 5 Rotor-related design variables and performance metrics for the mission optimization. FOM is figure of merit, as defined in Sec. III.A.4, and OEI is one engine inoperative.

C. Mission, rotor propeller distribution, rotor radius, and wing area

The values of the design variables and key quantities of interest are shown in Tab. 8 and 9. Trends for system-level parameters versus cruise speed again show agreement to those seen in the mission only optimization. We see a decrease of 9.66% in total power for the nominal hover condition, slightly higher than that of optimizing solely the operational variables and propeller twist profile. The one engine inoperable condition also sees a slight improvement with a decrease of 6.25%. Looking at the drawbacks for the cruise missions, we observe a 0.6%, 0.8%, and 17.63% increase in total power for the nominal, reserve, and max speed cruise conditions respectively. Regarding solely total power required, it

Condition	Speed (m/s)	Alpha (deg)	Tail trim (deg)	L/D	C_L	C_D (counts)	Total power (kW)
Cruise	66.67	3.48	-5.88	14.84	0.58	387.44	72.45
Reserve	55.56	5.99	-5.95	16.06	0.83	516.08	58.04
Max. speed	73.76	2.44	-5.86	13.57	0.47	346.13	110.25
Hover	1.0		-7.59				221.53
Hover.OEI	1.0		-7.52				241.47

Table 6 System-level design variables and performance metrics for the optimized design.

is apparent that optimizing all design parameters simultaneously holds greater benefits overall as opposed to optimizing only blade twist profile for the design parameters.

Fig. 9 shows before and after optimization comparisons for the propeller twist distributions. The twist profile changes much more drastically for the tilt rotors due to being operative in both cruise and hover, with minor differences between the twist and full design optimization. For the fixed and rear rotors, the twist profile shape stays roughly the same, flattening the profile overall and maintaining a near exact distribution between the twist and full design optimization.

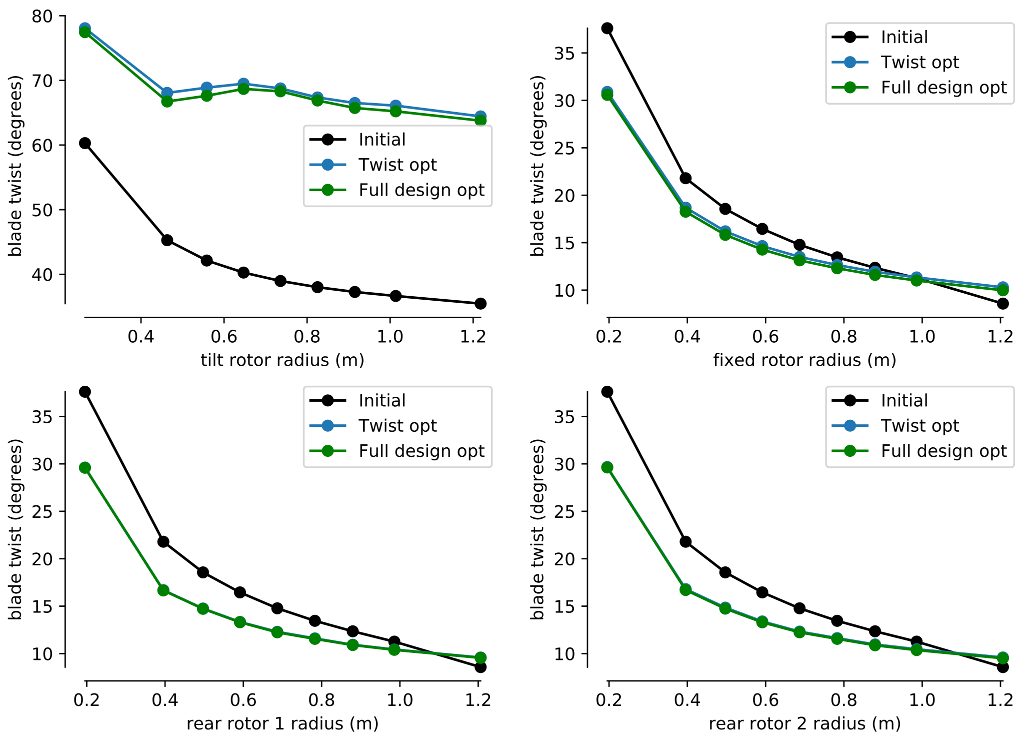

Fig. 9 Propeller blade twist distribution comparison across the optimization problems.

Fig. 10 compares relevant weight quantities between the optimization sets. The parameters between mission only

Condition	Rotor	RPM	Pitch (°)	Thrust (N)	Torque (Nm)	Power (kW)	Efficiency (%)
Cruise	tilt_rotor_left	364.6	55.0	486.2	948.9	36.2	89.5
Cruise	tilt_rotor_right	364.6	55.0	486.2	948.9	36.2	89.5
Cruise	fixed_rotor_left	983.6	0.0	-0.0	0.0	0.0	
Cruise	fixed_rotor_right	983.6	0.0	-0.0	0.0	0.0	
Cruise	rear_rotor_1	983.6	0.0	-0.0	0.0	0.0	
Cruise	rear_rotor_2	983.6	0.0	-0.0	0.0	0.0	
Reserve	tilt_rotor_left	331.4	55.0	466.9	836.1	29.0	89.4
Reserve	tilt_rotor_right	331.4	55.0	466.9	836.1	29.0	89.4
Reserve	fixed_rotor_left	983.6	0.0	-0.0	0.0	0.0	
Reserve	fixed_rotor_right	983.6	0.0	-0.0	0.0	0.0	
Reserve	rear_rotor_1	983.6	0.0	-0.0	0.0	0.0	
Reserve	rear_rotor_2	983.6	0.0	-0.0	0.0	0.0	
Max. speed	tilt_rotor_left	664.7	39.0	522.9	791.9	55.1	70.0
Max. speed	tilt_rotor_right	664.7	39.0	522.9	791.9	55.1	70.0
Max. speed	fixed_rotor_left	983.6	0.0	-0.0	0.0	0.0	
Max. speed	fixed_rotor_right	983.6	0.0	-0.0	0.0	0.0	
Max. speed	rear_rotor_1	983.6	0.0	-0.0	0.0	0.0	
Max. speed	rear_rotor_2	983.6	0.0	-0.0	0.0	0.0	
Condition	**Rotor**	**RPM**	**Pitch (°)**	**Thrust (N)**	**Torque (Nm)**	**Power (kW)**	**FOM (%)**
Hover	tilt_rotor_left	676.6	0.0	2451.7	637.1	45.1	49.0
Hover	tilt_rotor_right	676.6	0.0	2451.7	637.1	45.1	49.0
Hover	fixed_rotor_left	1608.0	-4.7	3526.3	320.6	54.0	102.2
Hover	fixed_rotor_right	1608.0	-4.7	3526.3	320.6	54.0	102.2
Hover	rear_rotor_1	1173.8	-5.0	1582.5	133.3	16.4	101.2
Hover	rear_rotor_2	876.7	-5.0	878.5	75.2	6.9	99.4
Hover.OEI	tilt_rotor_left	644.8	3.6	2696.7	816.3	55.1	46.3
Hover.OEI	tilt_rotor_right	644.8	3.6	2696.7	816.3	55.1	46.3
Hover.OEI	fixed_rotor_left	1607.0	-4.6	3566.7	326.6	55.0	102.1
Hover.OEI	fixed_rotor_right	1607.0	-4.6	3566.7	326.6	55.0	102.1
Hover.OEI	rear_rotor_1	983.6	15.0	0.0	0.0	0.0	
Hover.OEI	rear_rotor_2	1278.6	-5.0	1890.1	159.1	21.3	101.6

Table 7 Rotor and performance table for optimized mission and propeller twist distribution.

and the twist optimization is nearly identical, the decrease in gross weight being caused by the decreased sizing of the motors due to hover power minimization. The slight differences in wing weight and tail weight are due to their calculated dependence on the gross weight. With the full design optimization at work, we can see the optimizer chooses to decrease wing area by 3.89%, as seen in Tab. 10 which in turn leads to smaller propeller radii to satisfy spacing constraints.

Condition	Speed (m/s)	Alpha (deg)	Tail trim (deg)	L/D	C_L	C_D (counts)	Total power (kW)
Cruise	66.67	3.66	-6.19	15.04	0.59	391.19	71.3
Reserve	55.56	6.25	-6.4	16.18	0.85	523.92	57.09
Max. speed	73.76	2.59	-6.11	13.78	0.48	348.62	108.67
Hover	1.0		-7.63				217.41
Hover.OEI	1.0		-7.5				238.57

Table 8 System-level design variables and performance metrics for the optimized design.

Quantity	Value
Empty weight fraction	0.5
Battery weight fraction	0.22

Quantity	Value (lb)
Wing weight	448.44
Tail weight	76.0
Fuselage weight	280.23
Battery weight	728.45
Gross weight	3238.59

Quantity	Value
Empty weight fraction	0.5
Battery weight fraction	0.23

Quantity	Value (lb)
Wing weight	447.63
Tail weight	75.88
Fuselage weight	280.04
Battery weight	727.35
Gross weight	3226.6

Quantity	Value
Empty weight fraction	0.5
Battery weight fraction	0.22

Quantity	Value (lb)
Wing weight	432.2
Tail weight	75.58
Fuselage weight	279.57
Battery weight	715.37
Gross weight	3195.84

Fig. 10 Weight parameters for mission optimization (left), mission and twist (center), and all design variables (right).

D. Uncertainty quantification

Results of optimizing with uncertainties being considered are shown in Fig. 11. In order to produce more robust designs, the average total power increases as dependence on robustness increases as expected. With $a = 1.0$, meaning the optimizer cares solely on minimizing total power in the hover condition, the mean total power across the 7 conditions increases by only 0.492% when $a = 0.5$. The variance at $a = 1.0$ begins at 6111.76 W (too large to plot with other values), and drops 99.97% once a is decreased to 0.5. Even a small step at $a = 0.9$ shows a sharp decline in variance with relatively no gain in total power necessary. Therefore, major improvements to robustness may be made to the design while sacrificing low costs of total power for hover segments.

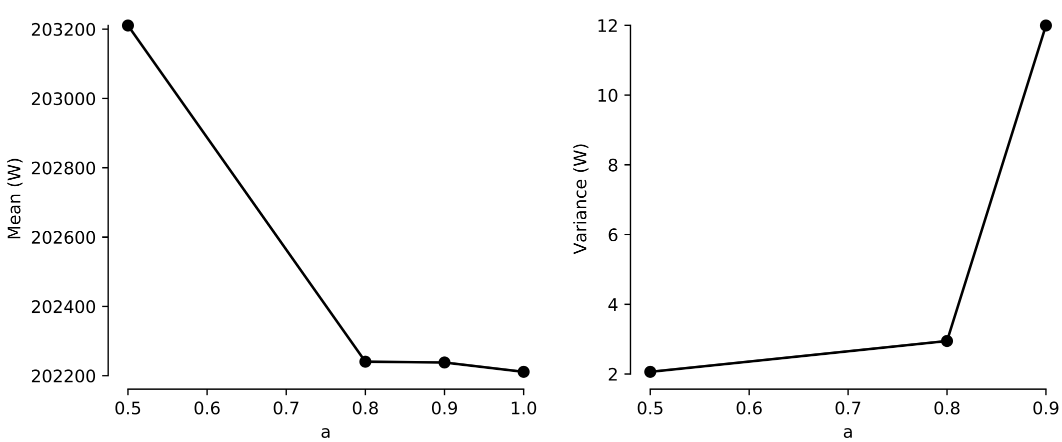

Fig. 11 Mean and variance in total power across varying weights of a.

Condition	Rotor	RPM	Pitch (°)	Thrust (N)	Torque (Nm)	Power (kW)	Efficiency (%)
Cruise	tilt_rotor_left	371.4	55.0	474.0	916.6	35.7	88.6
Cruise	tilt_rotor_right	371.4	55.0	474.0	916.6	35.7	88.6
Cruise	fixed_rotor_left	983.6	0.0	-0.0	0.0	0.0	
Cruise	fixed_rotor_right	983.6	0.0	-0.0	0.0	0.0	
Cruise	rear_rotor_1	983.6	0.0	-0.0	0.0	0.0	
Cruise	rear_rotor_2	983.6	0.0	-0.0	0.0	0.0	
Reserve	tilt_rotor_left	336.3	55.0	457.7	810.5	28.5	89.1
Reserve	tilt_rotor_right	336.3	55.0	457.7	810.5	28.5	89.1
Reserve	fixed_rotor_left	983.6	0.0	-0.0	0.0	0.0	
Reserve	fixed_rotor_right	983.6	0.0	-0.0	0.0	0.0	
Reserve	rear_rotor_1	983.6	0.0	-0.0	0.0	0.0	
Reserve	rear_rotor_2	983.6	0.0	-0.0	0.0	0.0	
Max. speed	tilt_rotor_left	660.9	39.9	508.6	785.0	54.3	69.0
Max. speed	tilt_rotor_right	660.9	39.9	508.6	785.0	54.3	69.0
Max. speed	fixed_rotor_left	983.6	0.0	-0.0	0.0	0.0	
Max. speed	fixed_rotor_right	983.6	0.0	-0.0	0.0	0.0	
Max. speed	rear_rotor_1	983.6	0.0	-0.0	0.0	0.0	
Max. speed	rear_rotor_2	983.6	0.0	-0.0	0.0	0.0	

Condition	Rotor	RPM	Pitch (°)	Thrust (N)	Torque (Nm)	Power (kW)	FOM (%)
Hover	tilt_rotor_left	689.8	0.0	2436.5	613.7	44.3	49.4
Hover	tilt_rotor_right	689.8	0.0	2436.5	613.7	44.3	49.4
Hover	fixed_rotor_left	1608.0	-4.5	3482.7	314.1	52.9	102.3
Hover	fixed_rotor_right	1608.0	-4.5	3482.7	314.1	52.9	102.3
Hover	rear_rotor_1	1168.3	-5.0	1563.5	131.4	16.1	101.3
Hover	rear_rotor_2	875.6	-4.9	876.9	75.0	6.9	99.5
Hover.OEI	tilt_rotor_left	633.3	4.7	2656.6	819.3	54.3	45.9
Hover.OEI	tilt_rotor_right	633.3	4.7	2656.6	819.3	54.3	45.9
Hover.OEI	fixed_rotor_left	1607.2	-4.3	3550.5	324.0	54.5	102.2
Hover.OEI	fixed_rotor_right	1607.2	-4.3	3550.5	324.0	54.5	102.2
Hover.OEI	rear_rotor_1	983.6	15.0	0.0	0.0	0.0	
Hover.OEI	rear_rotor_2	1272.6	-5.0	1864.5	156.5	20.9	101.7

Table 9 Rotor and performance table for optimized mission, propeller twist distribution, propeller radius, and wing size.

V. Conclusion

In this paper, we apply large-scale multidisciplinary optimization to obtain a design for an electric vertical takeoff and landing (eVTOL) aircraft. A primary objective is to complete system-level optimizations using different sets of design variables and observe differences in performance and design. Another objective is to evaluate uncertainty parameters and produce a design that is both efficient and robust.

First, we see system-level optimization incorporating mission, aerodynamics, propulsion, weights, and stability feasible, with reasonable convergence when observing decreases in optimality and feasibility. By using multi-point

Setup	tilt rotors radius (m)	fixed rotors radius (m)	rear rotor 1 radius (m)	rear rotor 2 radius (m)	wing projected area (m^2)
Initial	1.3689	1.3689	1.3689	1.3689	10.54
Full design opt	1.3415	1.3415	1.3689	1.3689	10.13

Table 10 High level design parameters for the initial and optimized design.

optimization, operational variables can be reasonably determined and provide insight to design choices at a conceptual level. Given additional computational resources, optimizations containing entire mission profiles can be simultaneously determined to evaluate design feasibility.

Second, when evaluating the three optimizations with increasing sets of design variables, we see 9.66% decrease in total power for the nominal hover case. This is an improvement to the optimization case where only operational variables and propeller twist distribution are varied. Due to optimizing solely to minimize nominal hover, both additional optimizations yield increases in total power required for the cruise segments; however, the full design optimization shows diminished drawbacks compared to that of the twist optimization case. As a result, to maximize efficiency for hover conditions, which dominate the max power required across the different possible mission points, the observed decrease in wing size is suggested to be advantageous for this type of eVTOL design.

Third, when accounting for uncertainty in the model, using a thrust power margin in our study, we see significant improvements can be made to the design's robustness at relatively minimal cost of efficiency. While only one distribution of uncertainties was examined, it highlights both the flexibility that the propeller design offers in the hover condition as well as the power of using an MDO approach to obtain proficient designs.

There is significant room for improvement using this model. The first step would be to combine the full design optimization along with the uncertainty distribution optimizations to simultaneously produce a robust design applicable for both hover and cruise missions. This would require either additional computational resources or improvements in the computation speed using accurate lower-fidelity models. Another area is a motor model that can capture the relationship between the propeller performance and motor sizing, as this in turn affects the weight distribution which sizes the aircraft altogether. With additional refined analysis models, the validity of optimization results can be improved and applied for use in eVTOL design for urban air mobility.

VI. Acknowledgements

The authors gratefully acknowledge support from Hyundai Motor Company (HMC). The third author also served as a consultant for HMC. The terms of this arrangement have been reviewed and approved by the University of California San Diego in accordance with its conflict of interest policies.

References

[1] Brelje, B. J., and Martins, J. R., "Electric, hybrid, and turboelectric fixed-wing aircraft: A review of concepts, models, and design approaches," *Progress in Aerospace Sciences*, 2018.

[2] Cramer, E. J., Dennis, J. E., Jr, Frank, P. D., Lewis, R. M., and Shubin, G. R., "Problem formulation for multidisciplinary optimization," *SIAM Journal on Optimization*, Vol. 4, No. 4, 1994, pp. 754–776.

[3] Borer, N. K., and Moore, M. D., "Integrated propeller-wing design exploration for distributed propulsion concepts," *53rd AIAA Aerospace Sciences Meeting*, 2015, p. 1672.

[4] Moore, K. R., and Ning, A., "Distributed Electric Propulsion Effects on Existing Aircraft Through Multidisciplinary Optimization," *2018 AIAA/ASCE/AHS/ASC Structures, Structural Dynamics, and Materials Conference*, 2018, p. 1652.

[5] Hwang, J. T., and Ning, A., "Large-scale multidisciplinary optimization of an electric aircraft for on-demand mobility," *2018 AIAA/ASCE/AHS/ASC Structures, Structural Dynamics, and Materials Conference*, 2018, p. 1384.

[6] Liang, C., and Mahadevan, S., "Bayesian framework for multidisciplinary uncertainty quantification and optimization," *16th AIAA Non-Deterministic Approaches Conference*, 2014, p. 1499.

[7] Crespo, L. G., Kenny, S. P., and Giesy, D. P., "The NASA Langley multidisciplinary uncertainty quantification challenge," *16th AIAA Non-Deterministic Approaches Conference*, 2014, p. 1347.

[8] Isikveren, A. T., Kaiser, S., Pornet, C., and Vratny, P. C., "Pre-design strategies and sizing techniques for dual-energy aircraft," *Aircraft Engineering and Aerospace Technology: An International Journal*, Vol. 86, No. 6, 2014, pp. 525–542.

[9] Courtin, C., and Hansman, R. J., "Safety Considerations in Emerging Electric Aircraft Architectures," *2018 Aviation Technology, Integration, and Operations Conference*, 2018, p. 4149.

[10] Heath, C., and Gray, J., "OpenMDAO: framework for flexible multidisciplinary design, analysis and optimization methods," *53rd AIAA/ASME/ASCE/AHS/ASC Structures, Structural Dynamics and Materials Conference 20th AIAA/ASME/AHS Adaptive Structures Conference 14th AIAA*, 2012, p. 1673.

[11] Martins, J. R., and Hwang, J. T., "Review and unification of methods for computing derivatives of multidisciplinary computational models," *AIAA journal*, Vol. 51, No. 11, 2013, pp. 2582–2599.

[12] Chaudhuri, A., Jasa, J., Martins, J., and Willcox, K. E., "Multifidelity Optimization Under Uncertainty for a Tailless Aircraft," *2018 AIAA Non-Deterministic Approaches Conference*, 2018, p. 1658.

[13] Yao, W., Guo, J., Chen, X., and Van Tooren, M., "Utilizing uncertainty multidisciplinary design optimization for conceptual design of space systems," *8th Annual Conference on Systems Engineering Research, CSER 2010, Hoboken, NJ, USA, 17-19 March 2010*, 2010.

[14] Yao, W., Chen, X., Luo, W., van Tooren, M., and Guo, J., "Review of uncertainty-based multidisciplinary design optimization methods for aerospace vehicles," *Progress in Aerospace Sciences*, Vol. 47, No. 6, 2011, pp. 450–479.

[15] Jaeger, L., Gogu, C., Segonds, S., and Bes, C., "Aircraft multidisciplinary design optimization under both model and design variables uncertainty," *Journal of Aircraft*, Vol. 50, No. 2, 2013, pp. 528–538.

[16] Vazquez, R., and Rivas, D., "Propagation of initial mass uncertainty in aircraft cruise flight," *Journal of Guidance, Control, and Dynamics*, Vol. 36, No. 2, 2013, pp. 415–429.

[17] Hu, X., Chen, X., Parks, G. T., and Yao, W., "Review of improved Monte Carlo methods in uncertainty-based design optimization for aerospace vehicles," *Progress in Aerospace Sciences*, Vol. 86, 2016, pp. 20–27.

[18] Peherstorfer, B., Beran, P. S., and Willcox, K. E., "Multifidelity Monte Carlo estimation for large-scale uncertainty propagation," *2018 AIAA Non-Deterministic Approaches Conference*, 2018, p. 1660.

[19] Hwang, J. T., Jasa, J. P., and Martins, J. R., "High-fidelity design-allocation optimization of a commercial aircraft maximizing airline profit," *Journal of Aircraft*, Vol. 56, No. 3, 2019, pp. 1164–1178.

[20] Anderson Jr, J. D., *Fundamentals of aerodynamics*, McGraw-Hill Education, 2010.

[21] Ning, S., *CCBlade documentation*, National Renewable Energy Laboratory, 2013.

[22] Veldhuis, L. L. M., "Propeller wing aerodynamic interference," 2005.

[23] Conway, J. T., "Analytical solutions for the actuator disk with variable radial distribution of load," *Journal of Fluid Mechanics*, Vol. 297, 1995, pp. 327–355.

[24] Alba, C., Elham, A., German, B., and Veldhuis, L. L., "A surrogate-based multi-disciplinary design optimization framework exploiting wing-propeller interaction," *18th AIAA/ISSMO Multidisciplinary Analysis and Optimization Conference*, 2017, p. 4329.

[25] Raymer, D. P., *Aircraft Design: A Conceptual Approach*, 5th ed., AIAA, 2012.

[26] Borer, N. K., Derlaga, J. M., Deere, K. A., Carter, M. B., Viken, S., Patterson, M. D., Litherland, B., and Stoll, A., "Comparison of Aero-Propulsive Performance Predictions for Distributed Propulsion Configurations," *55th AIAA Aerospace Sciences Meeting*, 2017, p. 0209.

[27] Deere, K. A., Viken, S., Carter, M., Viken, J. K., Derlaga, J. M., and Stoll, A. M., "Comparison of high-fidelity computational tools for wing design of a distributed electric propulsion aircraft," *35th AIAA Applied Aerodynamics Conference*, 2017, p. 3925.

[28] Hahn, A., "Vehicle sketch pad: a parametric geometry modeler for conceptual aircraft design," *48th AIAA Aerospace Sciences Meeting Including the New Horizons Forum and Aerospace Exposition*, 2010, p. 657.

[29] Gill, P. E., Murray, W., and Saunders, M. A., "SNOPT: An SQP algorithm for large-scale constrained optimization," *SIAM review*, Vol. 47, No. 1, 2005, pp. 99–131.

[30] Perez, R. E., Jansen, P. W., and Martins, J. R., "pyOpt: a Python-based object-oriented framework for nonlinear constrained optimization," *Structural and Multidisciplinary Optimization*, Vol. 45, No. 1, 2012, pp. 101–118.